



## RESEARCH ARTICLE

10.1029/2022JG006794

## Key Points:

- In Louisiana from 1984 to 2020, we estimated 1940.9 km<sup>2</sup> of wetland loss at a 53.9 km<sup>2</sup>/year rate (net change −1253.1 km<sup>2</sup> and −34.8 km<sup>2</sup>/year)
- We used machine learning to develop a remote sensing-based model that directly estimates soil accretion rates in coastal wetlands
- Accretion rates have significantly declined in the coastal basins that have lost the most wetland area

## Correspondence to:

D. J. Jensen,  
daniel.j.jensen@jpl.nasa.gov

## Citation:

Jensen, D. J., Cavanaugh, K. C., Thompson, D. R., Fagherazzi, S., Cortese, L., & Simard, M. (2022). Leveraging the historical Landsat catalog for a remote sensing model of wetland accretion in coastal Louisiana. *Journal of Geophysical Research: Biogeosciences*, 127, e2022JG006794. <https://doi.org/10.1029/2022JG006794>

Received 12 JAN 2022  
Accepted 23 MAY 2022

## Author Contributions:

**Conceptualization:** D. J. Jensen, K. C. Cavanaugh  
**Data curation:** D. J. Jensen  
**Formal analysis:** D. J. Jensen, M. Simard  
**Funding acquisition:** D. J. Jensen, M. Simard  
**Investigation:** D. J. Jensen, K. C. Cavanaugh, D. R. Thompson, S. Fagherazzi, L. Cortese, M. Simard  
**Methodology:** D. J. Jensen, K. C. Cavanaugh, D. R. Thompson, M. Simard  
**Project Administration:** D. J. Jensen, M. Simard  
**Resources:** D. J. Jensen  
**Software:** D. J. Jensen

## Leveraging the Historical Landsat Catalog for a Remote Sensing Model of Wetland Accretion in Coastal Louisiana

D. J. Jensen<sup>1,2</sup> , K. C. Cavanaugh<sup>3</sup>, D. R. Thompson<sup>1</sup> , S. Fagherazzi<sup>4</sup> , L. Cortese<sup>4</sup> , and M. Simard<sup>1</sup>
<sup>1</sup>NASA Jet Propulsion Laboratory, California Institute of Technology, Pasadena, CA, USA, <sup>2</sup>NASA Postdoctoral Program, Universities Space Research Association, Columbia, MD, USA, <sup>3</sup>Department of Geography, University of California Los Angeles, Los Angeles, CA, USA, <sup>4</sup>Department of Earth and Environment, Boston University, Boston, MA, USA

**Abstract** A wetland's ability to vertically accrete—capturing sediment and biological matter for soil accumulation—is key for maintaining elevation to counter soil subsidence and sea level rise. Wetland soil accretion is comprised of organic and inorganic components largely governed by net primary productivity and sedimentation. Sea level, land elevation, primary productivity, and sediment accretion are all changing across Louisiana's coastline, destabilizing much of its wetland ecosystems. In coastal Louisiana, analysis from 1984 to 2020 shows an estimated 1940.858 km<sup>2</sup> of total loss at an average rate of 53.913 km<sup>2</sup>/year. Here we hypothesize that remote sensing timeseries data can provide suitable proxies for organic and inorganic accretionary components to estimate local accretion rates. The Landsat catalog offers decades of imagery applicable to tracking land extent changes across coastal Louisiana. This dataset's expansiveness allows it to be combined with the Coastwide Reference Monitoring System's point-based accretion data. We exported normalized difference vegetation index (NDVI) and red-band surface reflectance data for every available Landsat 4–8 scene across the coast using Google Earth Engine. Water pixels from the red-band were transformed into estimates of total suspended solids to represent sediment deposition—the inorganic accretionary component. NDVI values over land pixels were used to estimate bioproductivity—representing accretion's organic component. We then developed a Random Forest regression model that predicts wetland accretion rates ( $R^2 = 0.586$ , MAE = 0.333 cm/year). This model can inform wetland vulnerability assessments and loss predictions, and is to our knowledge the first remote sensing-based model that directly estimates accretion rates in coastal wetlands.

**Plain Language Summary** Soil accretion in coastal wetlands—whereby a wetland area builds its surface by capturing sediment and organic matter—helps counter land loss due to the compaction of soil and sea level rise. Coastal Louisiana has seen significant coastal wetland loss due widespread coastal engineering altering the processes that impact accretion. Remote sensing data can represent these processes, including organic matter production and sediment deposition, but they have not before been applied to directly model accretion rates. Here, we use Landsat timeseries data to model accretion based on derived estimates of suspended sediment availability and bioproductivity. These remote sensing inputs represent the primary inorganic and organic accretionary components, respectively. We additionally track changes in Louisiana's coastal wetland extent from 1984 to 2020 for comparison to our estimated accretion rates, estimating a total of 1940.858 km<sup>2</sup> of total loss with a net change accounting for land gain of −1253.130 km<sup>2</sup> at a rate of −34.809 km<sup>2</sup>/year. Our machine learning model results show significant accretion rate declines in coastal regions that experienced the greatest loss over the study period. Our remote sensing-based model can inform future assessments of wetland vulnerability and loss predictions.

## 1. Introduction

Louisiana's coastal wetlands are undergoing extreme changes, with widespread conversion of almost 4,000 km<sup>2</sup> to open water since 1956 (Barras et al., 2003; Twilley et al., 2016). Sea level, land elevation, primary productivity, and sediment deposition have all seen historical fluctuations across Louisiana's coastline, destabilizing much of the coast's wetland ecosystems. While the Mississippi River Deltaic Plain (MRDP) has seen significant wetland loss due to the development of petroleum fields and land reclamation for agriculture (Morton et al., 2006), the wetlands' widespread isolation from the river network has caused the most significant ongoing degradation (Day et al., 2007). Prior to its extensive engineering, a natural network of distributaries flowed through the MRDP

**Supervision:** D. J. Jensen, K. C. Cavanaugh, M. Simard  
**Validation:** D. J. Jensen, D. R. Thompson  
**Visualization:** D. J. Jensen, M. Simard  
**Writing – original draft:** D. J. Jensen  
**Writing – review & editing:** D. J. Jensen, K. C. Cavanaugh, D. R. Thompson, S. Fagherazzi, L. Cortese, M. Simard

and delivered fresh water and sediments to adjacent wetlands during flood periods (Kim et al., 2009). As the Mississippi River system is now highly channelized with reinforced levees and there an additional 15,000 km of canals and associated spoil banks that cut across the deltaic plain and impede sheet flow of water through adjacent wetlands, the natural sediment supply to these wetlands is largely diminished or disassociated (Day et al., 2007). Additionally, relative sea level rise (RSLR)—the combined rate of eustatic sea level rise and ground subsidence—is driving wetland vegetation dieback and submergence throughout much of the coast. In addition to increased flood periods (Day et al., 2021), RSLR is increasing coastal wetland surface salinity rates, in turn decreasing wetland productivity and carbon accumulation rates (Baustian et al., 2017). At current rates of wetland loss, the overall carbon burial rate in coastal Louisiana may be reduced to 2.1 Tg total carbon per year, down 50% from the region's estimated 2013 carbon sequestration rate (Baustian et al., 2021). While much of Louisiana's coastal wetlands are degrading and submerging, the concentration of the Mississippi River's flow through its leveed main channel and the Atchafalaya River—its primary remaining distributary, which takes approximately 31% of the Mississippi River's total sediment discharge (Allison et al., 2012; Twilley et al., 2016)—has resulted in regimes of both wetland degradation and aggradation along Louisiana's coast. Accordingly, rates of sediment deposition and bioproductivity vary widely across Louisiana's coastal wetlands depending on local hydrogeomorphology, resulting in significant land building in the Mississippi “bird's foot” delta and the Atchafalaya Basin contrasting the widespread degradation and loss in the two complexes.

A wetland's ability to maintain its surface elevation is largely governed by the relationships between sea level, land elevation, vegetation type, primary productivity, and sediment deposition (Morris et al., 2002; Mudd et al., 2009). Coastal engineering, climate change, and RSLR have caused widespread changes in these factors across Louisiana, impacting the state's coastal wetland accretion rates. A wetland's ability to vertically accrete—meaning the capture of sediment and biological matter for soil accumulation—and maintain its elevation can be broken down into organic and inorganic components that comprise bioproductivity and sedimentation rates (FitzGerald et al., 2008). Sedimentation sees waterborne mineral sediment deposited as water inundates and flows through marshland, contributing to its vertical accretion. Additionally, tidal sedimentation is driven by suspended sediment loads interacting with tidal currents, typically delivered by the ecosystem's fluvial systems and are further impacted by rainfall-induced resuspension of sediment, wave action, and episodic storm activity (FitzGerald et al., 2008). On short timescales, storms induce flooding that deliver sediments to wetland vegetation, a process that has been shown to stabilize otherwise eroding coastal wetland areas (Goodbred & Hine, 1995). Storm-driven sedimentation can be especially important for wetland vegetation in high tidal frames that otherwise receive little flooding (Goodwin & Mudd, 2019) and wetland systems with little to no fluvial sediment input (Tognin et al., 2021). Over longer climatic timescales, then, rising sea levels augment accretion rates as wetlands alter bioproductivity to maintain their elevational equilibrium (Breda et al., 2020; Morris et al., 2002). Tidal amplitude determines the vertical range over which particular vegetation species can grow, while growth rates in turn have a direct positive relationship with tidal amplitude (Morris et al., 2012). Each species' accretion rate has a unique response to water elevation change, whereby it reaches peak productivity and accretion at an optimum SLR rate but faces declining accretion and eventual submergence at SLR rates beyond the optimum value (Morris et al., 2002; Mudd et al., 2009). Those species that have the greatest growth range with respect to tide level see the greatest elevational stability with respect to changes in sea level and suspended sediment loads within the wetland's constituent waterbodies (Kirwan & Guntenspergen, 2010). Patterns of flooding duration and depth, in concert with sediment supply, accordingly exert significant control on wetland and productivity, and thereby their stability and carbon storage potential.

Wetland plant bioproductivity, then, contributes to organic peat production, forming the primary biological accretionary component. Direct contribution to wetland soil levels occurs as organic plant matter is deposited, trapped, and partially decomposed within the soil layer. The permanent burial and storage of carbon, then, is equivalent to the product of a plant's roots, rhizomes, and the fraction of organic matter that is resistant to decay, with wetlands' peraquatic moisture regimes and anaerobic soils limiting decomposition and fostering carbon sequestration (Morris et al., 2012; Mudd et al., 2009). This is in part because the annual root and rhizome production in wetland vegetation governs its belowground turnover rate, depositing plant matter directly into the soil. Indeed, organic matter accrual is the primary input by which wetlands may establish on the high end of their tidal frame, where they are least vulnerable to SLR and decreases in productivity (Kirwan & Megonigal, 2013). The deposited biomass stored within soils forms wetlands' most significant “blue carbon” sink, while wetland vegetation's biomass modulates its response to RSLR and its potential for inundation and loss (Chmura et al., 2003). In

addition to direct belowground turnover and deposition, vegetation biomass plays a key role in the exchange of sediments and carbon between inland regions and the coast, as they affect sediment attenuation and therefore accretion rates (Krauss et al., 2014). Following colonization, high initial rates of belowground production can stabilize loosely consolidated sub-aerial sediments in emergent wetlands, and further biomass accumulation above- and belowground then facilitates sediment trapping and attenuation, thereby stabilizing the marsh platform elevation (Cahoon et al., 2011). With regards to wetland restoration, it has been demonstrated that successful restoration projects are primarily driven by sediment availability (Liu et al., 2021), though vegetation cover, tidal amplitude, and relative land area are also associated with wetland stability due to their impacts on bioproductivity and contributions to accretion (Schoolmaster et al., 2018). Subsidence—being the compaction of subsurface material—is often exacerbated by local groundwater withdrawal, hydrocarbon extraction, tectonic activity, and reduced mineral sediment input (Burkett et al., 2003; Ericson et al., 2006). A wetland's vertical accretion rate must be greater than the underlying subsidence rate or submergence will occur over time. Ultimately, the interplay between these inorganic and organic accretionary factors determines a wetland's ability to counteract subsidence and keep pace with RSLR.

Accretion rates can vary widely across coastal regions, and coastal wetlands areas such as in Louisiana show a wide range in rates of submergence as a result. Many studies have incorporated remote sensing data and predictive models to address wetland loss and response to sea level rise but do not incorporate remotely sensed data products to account for accretionary processes at a regional scale. Ecological studies that account for accretion rates to predict wetland response to sea level rise are typically done based on discrete field data for modeling purposes (e.g., Morris et al., 2002; Mudd et al., 2009). Their results, then, are not easily transferrable to the regional scales that remote sensing data can address. Conversely, studies that incorporate spatial datasets to examine wetland changes typically do not employ direct inputs for sedimentation and bioproductivity to derive accretion rate estimates (e.g., Craft et al., 2009), instead relying on other spatial variables and proxies such as channel distance and fetch (a proxy for wave-driven sediment resuspension) to capture accretionary processes (Cortese & Fagherazzi, 2022). Remote sensing offers the ability to accurately model and map these factors that drive wetland accretion rates and thereby provide more accurate assessments of blue carbon storage and sequestration dynamics at regional and global scales. Within remote sensing science and its ecological applications, studies tend to focus on algorithm development or data product generation relevant to factors that influence vertical accretion rates in coastal wetlands. These application areas include shoreline extent and vegetation changes (Ragoonwalla et al., 2016; Roy et al., 2020; Zhange et al., 2021), bioproductivity (Byrd et al., 2018; Doughty and Cavanaugh, 2019; Thomas et al., 2019), and sediment loads (Dogliotti et al., 2015; Jensen et al., 2019; Pereira et al., 2018; Topp et al., 2020). As various products that may be estimated from remote sensing data pertain to accretionary processes—i.e., hydrologic sediment and vegetation characteristics—further analysis of those products in concert may yield insights into vertical accretion itself.

While remote sensing analyses have been conducted to monitor and estimate coastal wetland processes related to accretion, there has not to our knowledge been a published study that uses remotely sensed data to directly estimate accretion in coastal wetland environments. Here, we hypothesize that multispectral timeseries data can provide suitable proxies for organic (organic matter deposition pursuant to bioproductivity) and inorganic (fluvial and tidal sedimentation) accretionary components, and can thus be applied to estimate local accretion rates. We thus apply a machine learning approach to investigate how much of the variance in Louisiana's accretion record can be explained by these remotely sensed proxies.

## 2. Data and Methods

### 2.1. In Situ Accretion Data

The Louisiana Coastal Protection and Restoration Authority (CPRA) routinely measures accretion at wetland sites across the coast as part of its Coastwide Reference Monitoring System (CRMS; <https://lacoast.gov/crms/#>). These measurements show the rates of soil accretion or erosion (cm/year) at CRMS sites based on feldspar soil markers within herbaceous wetland or forested swamp areas at 6- or 12-month intervals. The accretion data were downloaded from the CPRA website (<https://cims.coastal.louisiana.gov/monitoring-data>), with accretion measurements spanning 8 March 2006–18 November 2019. Each sample site contains 1–4 accretion measurements with multiple sampling periods. The final accretion measurements at each site were divided by the timespan since establishment and averaged together to calculate site-specific average accretion rates. We subsequently



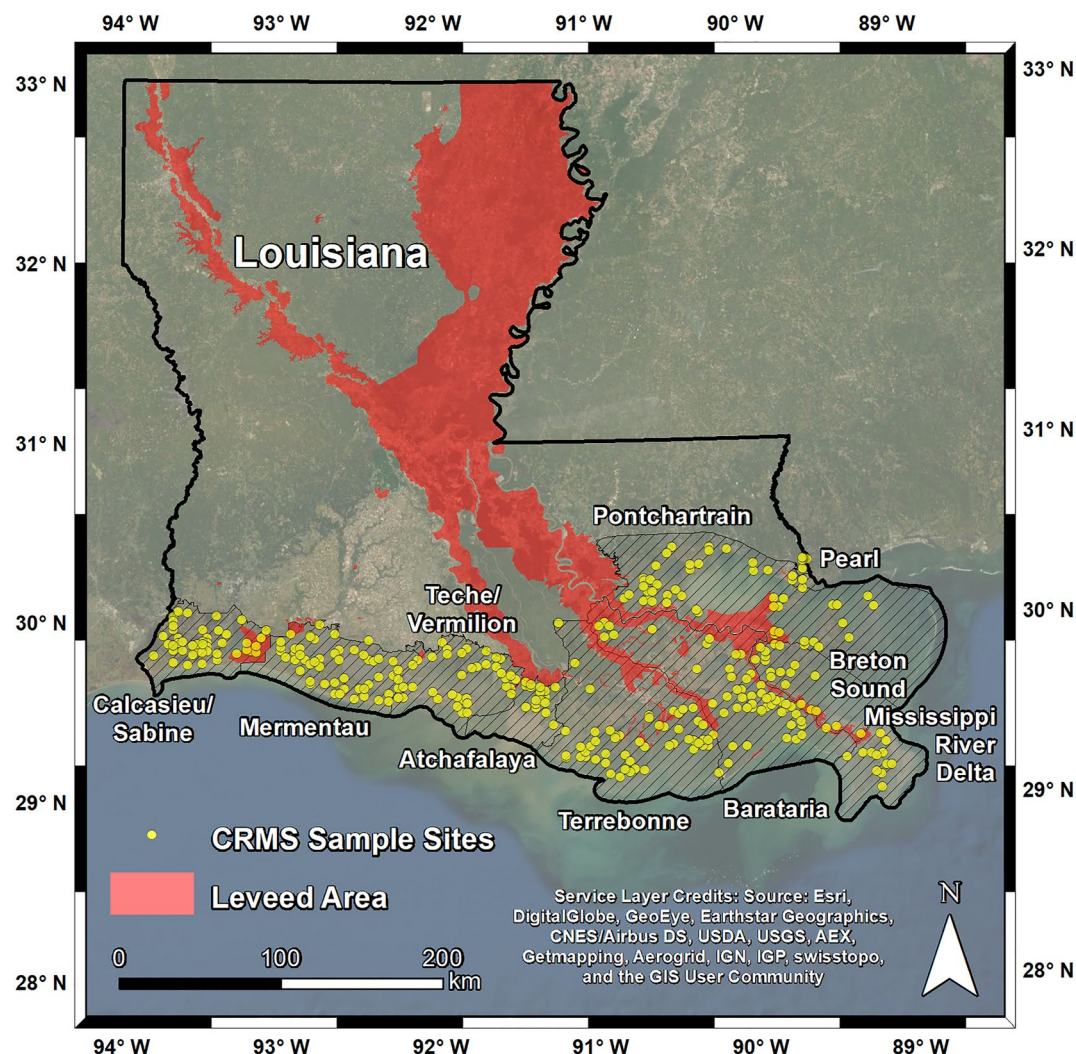


**Figure 1.** Study area in Louisiana's coastal basins, shown in hatching, and the distribution of the Coastwide Reference Monitoring System (CRMS) accretion sample data.

joined the accretion rate data with the corresponding CRMS site GIS point layer (Figure 1; <https://cims.coastal.louisiana.gov/viewer/metadata/crms6298.xml>). All resulting average points were carried forward into the model development.

## 2.2. Landsat Data

The Landsat catalog provides the most expansive and consistent moderate resolution remote sensing data with which to study proxies for accretionary processes over regional scales. The multispectral Landsat record, going back to the launch of Landsat 4 and its Thematic Mapper instrument in 1982, provides near-continuous visible-near-infrared (VNIR) global coverage. Recent advancements in cloud archiving and computing of remote sensing data have further enabled the processing and analysis of large timeseries data, with the Google Earth Engine platform hosting the entire Landsat catalog (<https://developers.google.com/earth-engine/datasets/catalog/landsat>). We thus used Google Earth Engine to process and collect 30m resolution data scenes from Landsat 5, 7, and 8 that encompassed all wetland areas across coastal Louisiana's hydrologic basins ([https://lacoast.gov/crms\\_viewer/Map/CRMSViewer](https://lacoast.gov/crms_viewer/Map/CRMSViewer)) across the 2006–2019 timespan matching the CRMS accretion record. These included cloud-masked surface reflectance products for all red band data and matching normalized difference vegetation index (NDVI) data. Across the seven Path/Row tiles assessed for the study period, 1,490 images for each of the NDVI and red band products were processed and exported.

### 2.3. Accretion Model Development

With the Landsat 5–8 archive temporally matching the CRMS accretion data compiled, we developed a machine learning model for accretion. In this model, the organic and inorganic processes of accretion—i.e., bioproductivity-driven organic matter deposition and fluvial/tidal sedimentation, respectively (FitzGerald et al., 2008)—were derived from the Landsat data and served as the independent variables.

#### 2.3.1. Suspended Sediment Concentration Model Selection

Spaceborne optical remote sensing enables the retrieval of information regarding optically active water constituents present in coastal waterbodies, including chromophoric dissolved organic matter (CDOM), phytoplankton, and measures of suspended sediment such as total suspended solids (TSS) (Griffin et al., 2011; Olmanson et al., 2013). The availability of satellite-borne multispectral sensors has led to the proliferation of algorithms for measuring suspended sediment concentrations that utilize its curvilinear relationship between VNIR (Neched et al., 2010; Chen et al., 2015). However, the composition and mixture of a waterbody's optically active constituents affect its inherent optical properties (IOPs), which in turn affect its observed reflectance signal in concert with instrument viewing geometry and illumination conditions (Mobley et al., 2010). The general applicability of a water quality model therefore must be tested to ensure retrievals are not significantly distorted by variation in the study area's IOPs. To that end, we identified four generalized models for deriving sediment concentration values from Landsat data, as assessed by Dorji and Fearn (2016) that were potentially applicable in our coastal Louisiana domain. Given how water constituents such as CDOM and chlorophyll content may impact algorithmic retrievals, we used in situ data collected in October 2016 to assess model applicability (Castaneda et al., 2020; Jensen et al., 2019, 2020). These data consisted of 35 TSS measurements from water surface samples paired with ASD FieldSpec® three water-leaving reflectance measurements. We then derived the relevant simulated band reflectance values for each sample by applying the corresponding Landsat band relative spectral response (RSR) function to the spectrometer data with Equation 1 (Chen et al., 2015):

$$R_{rs}(Bi) = \frac{\sum_{\lambda_1}^{\lambda_n} S(\lambda) R_s(\lambda)}{\sum_{\lambda_1}^{\lambda_n} S(\lambda)} \quad (1)$$

where  $\lambda_1$  and  $\lambda_n$  are the lower and upper limit wavelength of the Landsat band  $i$ ,  $S(\lambda)$  is the given band's spectral response function (<https://landsat.gsfc.nasa.gov/landsat-8/spectral-response-operational-land-imager-band-band-average-relative-spectral-response>), and  $R_s(\lambda)$  is the measured in situ reflectance. The assessed TSS models, each assessed by Dorji and Fearn (2016), are as follows:

$$\text{TSS} = \frac{400.75\rho(B1)}{1 - \rho_w(B1)/0.1774} + 1.02; \quad \rho_w(B1) = 0.539 \times \pi R_{rs}(B1) \quad (2)$$

$$\text{TSS} = 5.184 + 1349.63 R_{rs}(TM4) + 614561.673 [R_{rs}(TM4)]^2 \quad (3)$$

$$\text{TSS} = 8.602 + 1805.26 R_{rs}(TM4) + 900713.14 [R_{rs}(TM4)]^2 \quad (4)$$

$$\text{TSS} = \frac{289.29\rho_w(OLI4)}{1 - \rho_w(OLI4)/0.1686}; \quad \rho_w(OLI4) = 0.529 \times \pi \times R_{rs}(OLI4) \quad (5)$$

where  $\rho$  and  $\rho_w$  are the water-leaving reflectance for the designated Landsat band and  $R_{rs}$  is the remote sensing reflectance for given band. In applying Equations 2–4, we divided the standard water-leaving reflectances by  $\pi$  to calculate (Figure 1)  $R_{rs}$ .

With the relevant bands simulated for the four models from the in situ reflectance samples, we applied each and assessed resulting errors. TSS estimates were plotted against the water sample measurements to examine the distribution of errors relative to the 1:1 line, and we calculated the mean absolute error (MAE, mg/L) for each model (Figure 2). The TSS model developed by Vanhellemont and Ruddick (2014), trained in a survey in the United Kingdom's southern North Sea, showed lowest MAE at 9.67 mg/L and the closest adherence to the 1:1 line despite a bias of 8.683. As these errors are relatively low and the slope of the errors' line of best fit is close to 0—indicating minimal skew in the estimate values—we selected this generalized model to derive TSS estimates from the timeseries of the Landsat red band water pixels.

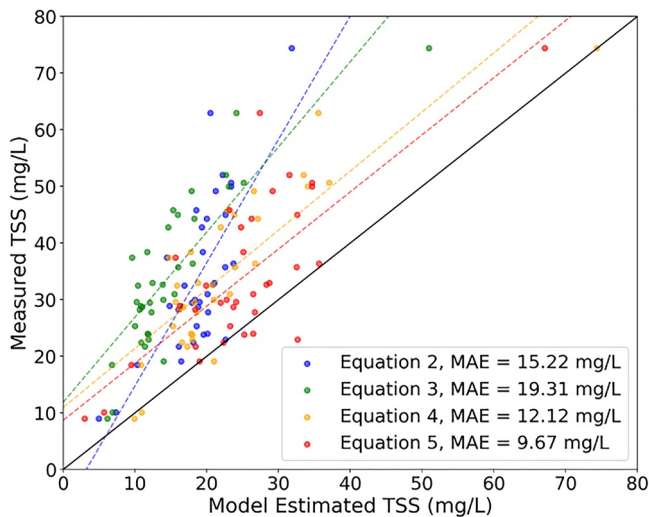


**Figure 2.** Error distributions of the assessed Landsat-based Total Suspended Solids (TSS, mg/L) retrieval models.

### 2.3.2. Landsat Timeseries Analysis

To combine the CRMS accretion data with corresponding Landsat timeseries data, we first joined the tabular accretion sample information with a GIS point layer of each CRMS site where the measurements were conducted. We then buffered the points by 1,000 m, creating a circular area around each point within which we aggregated the timeseries statistics. As each CRMS accretion sample includes dates for its first and last measurement, we temporally matched a collection of Landsat data to the sample period for each point. For each of the 347 points, we averaged all of the Landsat NDVI and red band surface reflectance data from the scenes that fell within the sample period. We then applied a two-cluster k-means classifier to the mean NDVI data, returning a water mask for the given point. The resulting water mask was used to mask the water pixels from the average NDVI and conversely mask the land pixels from the average red reflectance. Within the 1,000 m buffer, we extracted the average NDVI of the land pixels as a proxy for bioproductivity and organic matter deposition over the CRMS accretion sample period. Similarly, we applied the TSS model in Equation 5 (Vanhellemont & Ruddick, 2014) to the average red reflectance value of the water pixels within the 1,000 m buffer and calculated the average TSS as a proxy for sediment deposition at each site.

In addition to the average NDVI and TSS values for each CRMS site, we extracted average elevation and distance to water to introduce variables that account for the flow of sediment-bearing water to each accretion sample site. We used the water masks generated from the Landsat NDVI composites to calculate the Fast Marching Method (FMM) distance to water over the land pixels. However, levees throughout the coast prevent consistent delivery of fresh water bearing sediment into surrounding wetland areas. To incorporate this barrier in our model, we downloaded the US Army Corps of Engineers leveed area GIS data (<https://levees.sec.usace.army.mil/>) and rasterized it to be ingested in the FMM implementation as an obstacle that penalizes travel distance. The USGS National Elevation Dataset (2016, 1 arc-second resolution; <https://apps.nationalmap.gov/viewer/>) was also downloaded for the whole Louisiana coast and used to aggregate the elevation values at each site. In addition to these independent variables, we tested model performances incorporating wetland vegetation class (<https://cims.coastal.louisiana.gov/Viewer/GISDownload.aspx>) and the ratio of land:water pixels as measures of wetland type and fragmentation that may influence accretion rates. In total, mean NDVI, model-derived TSS, FMM distance, and elevation at each CRMS sample site were aggregated to develop the final accretion model.

### 2.3.3. Accretion Model Training, Validation, and Application

These aggregated data were ingested into a Random Forest regression model, with the CRMS accretion data being the dependent variable. Machine learning models such as Random Forest are well suited to these data, as they are capable of detecting and quantifying nonlinear relationships and interactions between the independent variables (Ryo & Rillig, 2017). First, the compiled data were filtered to remove outlier data points such that the maximum allowable accretion value was set at the 75th percentile value plus 1.5 times the interquartile range. Next, we employed a randomized search cross-validation function to determine the optimal hyperparameters for the model. These parameters (and their respective optimal settings) included the number of trees in the forest (400), the maximum number of features considered for splitting a node (20), the maximum number of levels in each decision tree (90), the minimum data points in a node before splitting (10), the minimum data point allowed in a leaf node (4), and bootstrapping (with replacement). We then trained the model on the 276 data points remaining after filtering the accretion sample outliers and discarding samples that did not have valid water pixels within their buffer zones. To validate the model, we employed an additional k-fold cross-validation scheme whereby we withheld one third of the data—a random selection of 92 samples—and trained the model on the remaining two thirds. This randomized cross-validation was simulated 100 times, and the resulting error distributions and metrics were averaged (Figure 3).

To apply the model to 2020 data, we generated mean NDVI and red reflectance data from Landsat 7 and 8 data for the growing season of March–October (Snedden et al., 2014) across the whole Louisiana coast again using Google Earth Engine. The model was then applied to the stacked raster data consisting of NDVI, TSS (using a



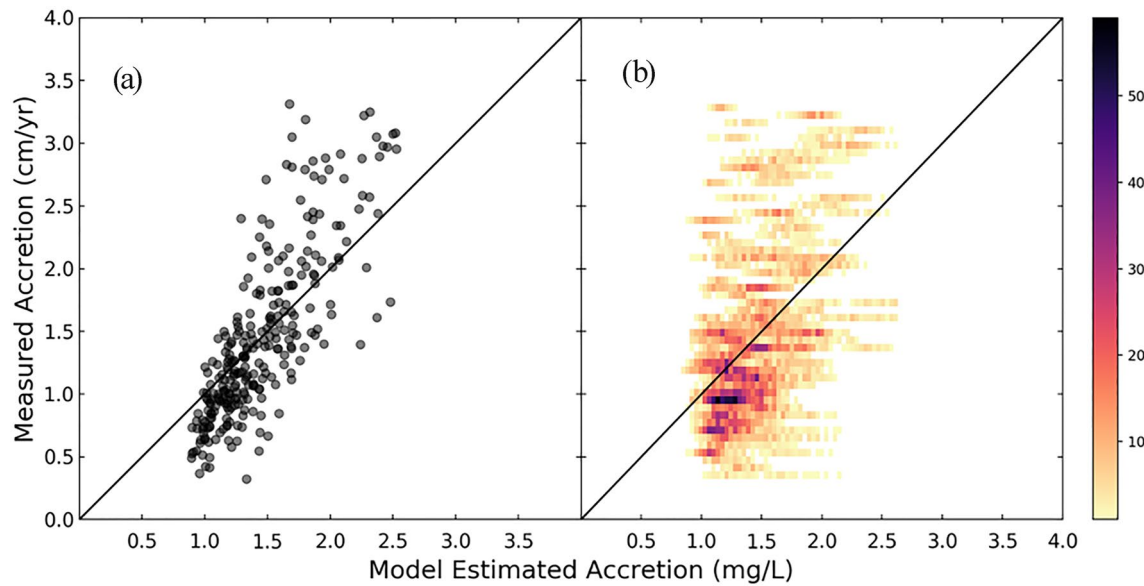


**Figure 3.** (a) Scatterplot of the 276 points predicted by model 8, plotting the measured accretion against the model estimated accretion. (b) Results of the 100 randomly selected cross-validations simulations shown in a 2D histogram.

search window of 100 pixels around each land pixel to estimate local sediment availability), FMM distance, and National Elevation Dataset DEM (Figure 4). The model was additionally applied to these products generated for the 1984–2019 growing seasons to construct a timeseries of estimated accretion rates across coastal Louisiana. We calculated the average accretion rate in each basin for all years and subsequently calculated the line of best fit for each basin to plot a trend of accretion rates over time.

Finally, to examine historical distributions of wetland loss and gain, we generated a land extent change map for our study area that spans 1984–2020. In addition to the 2020 mean NDVI product described above, we used

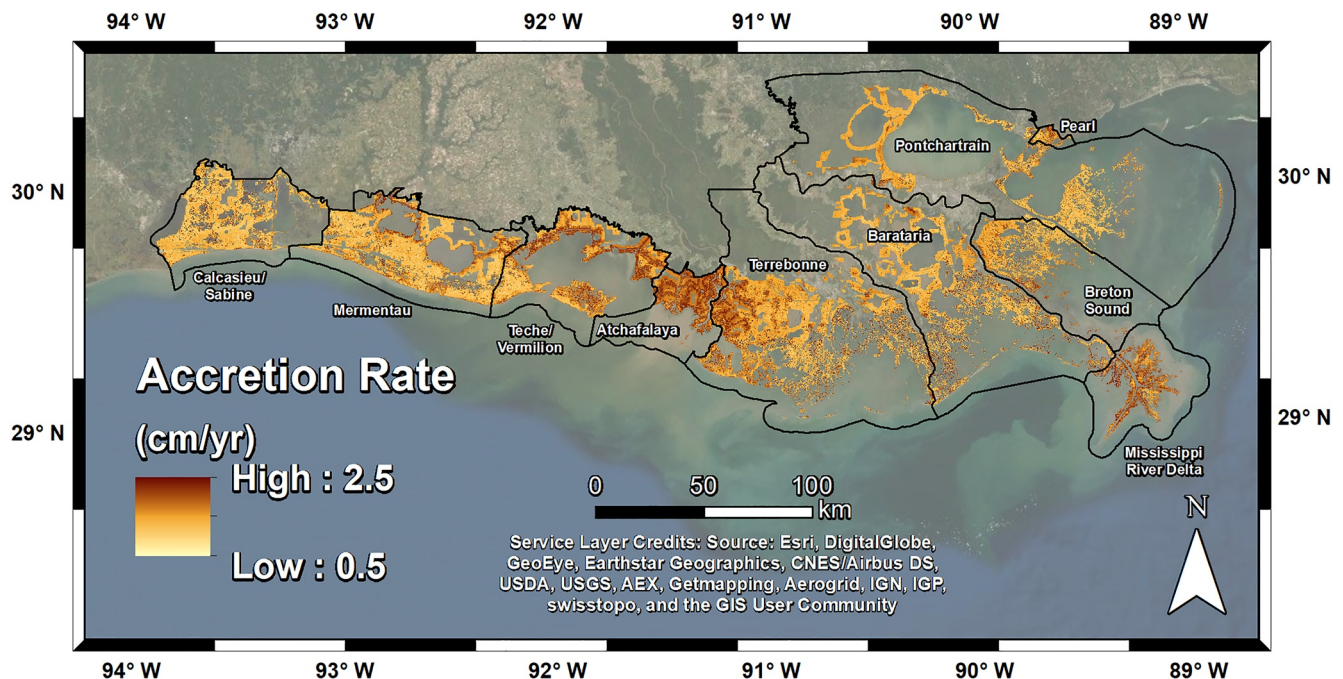


**Figure 4.** Predicted 2020 accretion rate map for coastal Louisiana, based on Landsat-derived mean growing season (March–October) NDVI and suspended sediment estimates.

**Table 1**  
*Accretion Model Performances*

Model variables	Model $R^2$	Model MAE (cm/year)	Feature importance scores	Validation mean $R^2$	Validation mean MAE (cm/year)
1. TSS, NDVI	0.500	0.374	0.421, 0.579	0.119	0.493
2. TSS, NDVI, distance	0.543	0.352	0.304, 0.369, 0.327	0.170	0.477
3. TSS, NDVI, class	0.482	0.374	0.374, 0.518, 0.108	0.127	0.494
4. TSS, NDVI, distance, class	0.586	0.329	0.277, 0.365, 0.297, 0.061	0.175	0.475
5. TSS, NDVI, Distance, L/W ratio	0.587	0.334	0.241, 0.323, 0.220, 0.216	0.142	0.494
6. TSS, NDVI, distance, L/W ratio, class	0.554	0.349	0.220, 0.280, 0.219, 0.223, 0.058	0.159	0.481
7. TSS, NDVI, FMM distance	0.565	0.344	0.304, 0.391, 0.305	0.182	0.479
8. TSS, NDVI, FMM distance, Elevation*	0.586	0.333	0.237, 0.355, 0.200, 0.208	0.198	0.466
9. TSS, NDVI, FMM distance, elevation, L/W ratio	0.581	0.336	0.211, 0.281, 0.156, 0.164, 0.188	0.170	0.485

Google Earth Engine to generate another composite NDVI from Landsat 4 and 5 data for the 1984 growing season. We applied a two-class k-means clustering algorithm to each of these datasets to classify land and water areas in each year. We also applied fractional floating and submerged aquatic vegetation (FAV and SAV) data calculated for each year to reduce potential confusion between land and water (Couvillion, 2021), classifying pixels with persistent FAV and SAV cover (over 20%) as water. By overlaying these 1984 and 2020 maps, we calculated changes in coastal land area that we could then compare with our accretion estimates.

### 3. Results

We assessed nine different models' performances with the Landsat-derived TSS and NDVI data in conjunction with various combinations of FMM distance, elevation, vegetation class, and land:water pixel ratio (Table 1). Each successive model, generally being in order of complexity, uses a different variable combination to test potential variable importances and interactions. We determined that model 8 (TSS, NDVI, FMM distance, and elevation) was best suited to predicting accretion rates in coastal Louisiana. The Random Forest model feature importance scores for these—0.237, 0.355, 0.200, and 0.208, respectively—contrast the scores attained by the models that incorporated wetland class, such that the class variable always attained a low score. Feature importance scores approximately sum to one and indicate each variable's contribution to the overall model's predictive power (Menze et al., 2009). The land/water pixel ratio variable attained similarly high feature importance scores, though with worse cross-validation results compared to models that applied the FMM distance and elevation instead.

Model 8 resulted in among the highest overall  $R^2$  values at 0.586, explaining 58.6% of the variance in the CRMS accretion record. It also attained amongst the lowest MAE values at 0.333 cm/year. It should be noted that we tested this model approach with Landsat-derived data extracted from only the March–October growing season rather than all available data. The model performed slightly worse ( $R^2 = 0.578$ , MAE = 0.338 cm/year), indicating that the overall model benefited from the increased sample size and potentially capturing relevant data during the senescent period. Other models attained similar overall error metrics upon parameterization. However, averaging the 100 randomized cross-validation simulations for each model showed that model 8 attained the highest average  $R^2$  and lowest MAE calculated from the validation sample subset in each simulation.

The accretion rate map derived from model 8 shows the variation in predicted rates across coastal Louisiana for the year 2020. To further investigate accretionary drivers and their distributions across Louisiana's coast, we calculated the average estimated 2020 accretion rates within each coastal basin. We concurrently calculated the basin-specific and total wetland area lost across the Landsat timeseries from 1984 to 2020. Overall, 1940.858 km<sup>2</sup> (53.913 km<sup>2</sup>/year) of wetland area have been lost, with a net change of −1253.130 km<sup>2</sup> (−34.809 km<sup>2</sup>/year) (Table 2, Figure 5). Accordingly, a linear regression with each basin's fractional land change from 1984 to 2020 (net areal change divided by total land area) as the dependent variable (y) and the corresponding 2020 mean estimated accretion rate as the independent variable (x) reveals a significant positive relationship (Figure 6b,  $R^2 = 0.630$ ,  $p = 0.006$ ). Additionally, the basins that underwent the greatest land loss over this period such as



**Table 2**  
*Land Change and Accretion Metrics Across Louisiana's Coastal Basins*

Basin	Land lost (km <sup>2</sup> , 1984–2020)	Land gained (km <sup>2</sup> , 1984–2020)	Net land change (km <sup>2</sup> , 1984–2020) [fractional land change]	Mean accretion rate (cm/year, 2020)
Calcasieu/Sabine	181.374	91.061	−90.313 [−0.049]	1.341
Mermentau	156.7917	28.020	−128.772 [−0.052]	1.429
Teche/Vermilion	80.860	17.897	−62.963 [−0.043]	1.660
Terrebonne	552.185	80.182	−472.003 [−0.134]	1.582
Atchafalaya	5.714	92.835	+87.121 [+0.155]	1.945
Barataria	525.134	55.768	−469.366 [−0.147]	1.475
Mississippi River Delta	111.858	224.440	+112.582 [+0.197]	1.857
Breton sound	141.697	71.286	−70.411 [−0.065]	1.512
Pontchartrain	181.715	25.835	−155.880 [−0.070]	1.414
Pearl	3.530	0.405	−3.125 [−0.039]	1.656
Total	1,940.858	687.728	−1253.130 [−0.074]	1.525

Terrebonne and Barataria show significant declining accretion trends, while more stable or prograding basins such as Teche/Vermilion and Atchafalaya show more stable trends (Figure 6a).

#### 4. Discussion

The estimated 2020 accretion map is in agreement with established patterns of sediment availability, bioproductivity, and land loss. Areas with high accretion rates are largely clustered around the river systems and distributaries where fresh water bears significant suspended sediment loads that flow through the surrounding wetland areas during flood periods (Twilley et al., 2016, 2019). These high accretion areas include the “bird’s foot” delta of the Mississippi River with an average accretion rate of 1.857 cm/year, and more significantly the Atchafalaya Basin where the Atchafalaya River and Wax Lake Outlet deposit in the Gulf of Mexico. The average 2020 accretion

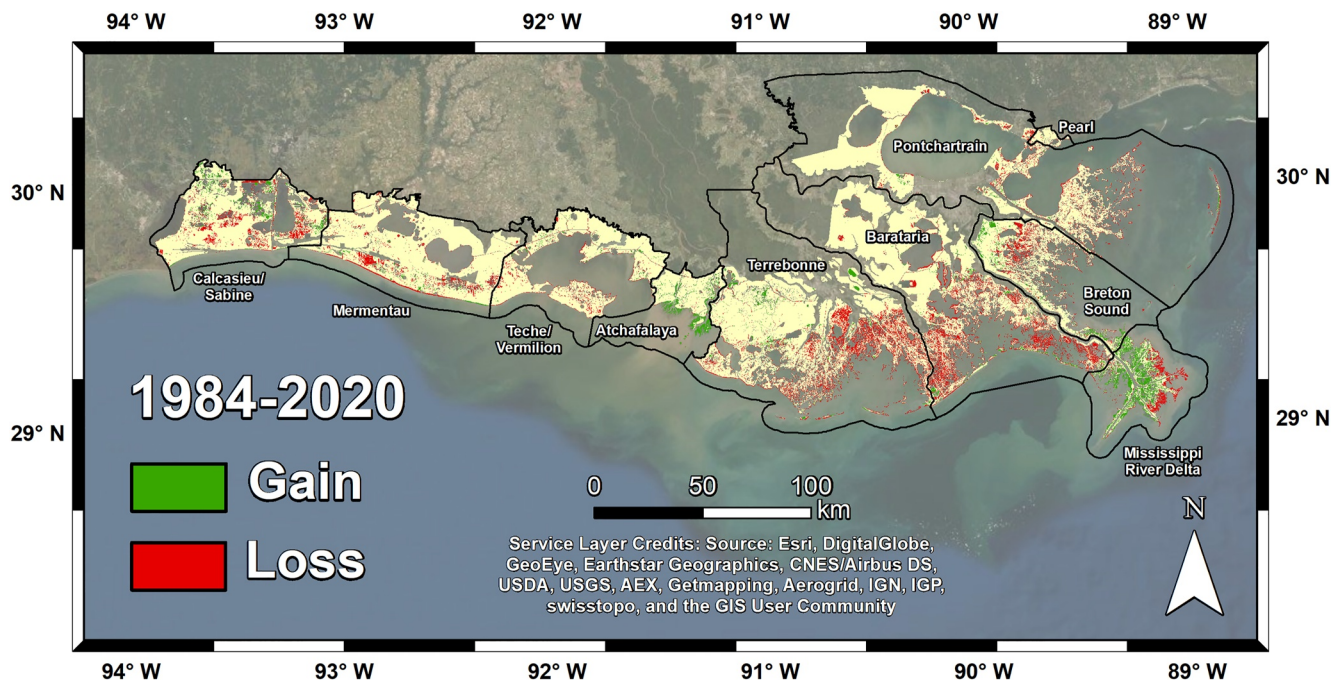


**Figure 5.** Land change from 1984 to 2020, based on k-means clustering of mean growing season (March–October) NDVI.

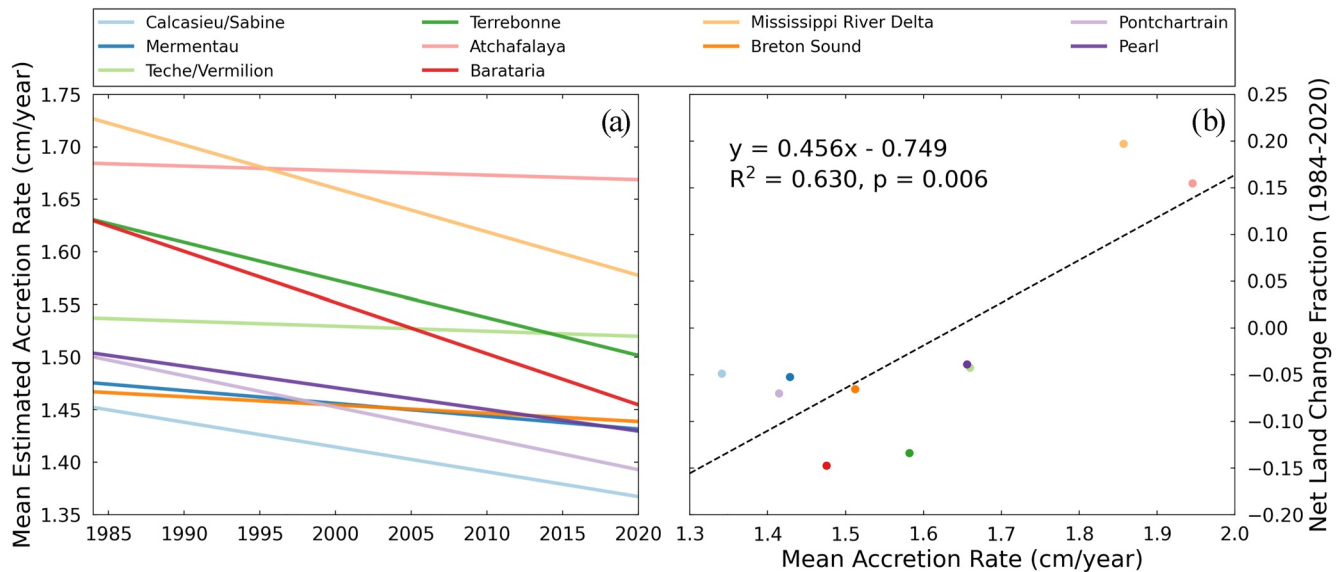


**Figure 6.** (a) Per-basin estimated accretion rate trend from 1984 to 2020. Lines are linear fits for each year's average accretion rate. (b) Scatterplot of the 2020 estimated mean accretion rates per basin and the net land area change fraction from 1984 to 2020.

rate in this basin is the highest in coastal Louisiana (1.945 cm/year) and is accordingly associated with this basin experiencing the second most land gain at 92.835 km<sup>2</sup> from 1984 to 2020, following the Mississippi River Delta itself at 224.440 km<sup>2</sup> (Table 2, Figure 5). These two regions are the only basins that experienced net land gain, which is a direct result of the widespread engineering of the broader deltaic plain leaving the bird's foot delta and the Atchafalaya River/Wax Lake Outlet as the primary remaining distributaries for the whole river system (Kim et al., 2009). The mean estimated 2020 accretion rates in these basins are correspondingly high, being the only basins above 1.7 cm/year (Table 2), due to the high levels of fluvial sediment deposition. Fluvial sedimentation, whereby river waters periodically flow through wetland vegetation and deposit their suspended mineralogic sediments, historically occurred throughout a natural network of distributaries in the deltaic plain but is now largely constrained (Olson & Suski, 2021; Twilley et al., 2016). The lack of sediment deposition in Louisiana's other coastal basins is directly related to their net land loss.

These hydrologic changes have also made much of Louisiana's coastal wetland areas more saline, with the resulting wetland species that tolerate a more brackish environment being overall less bioproductive than their freshwater counterparts (Song et al., 2011). Additionally, brackish marshes largely erode at higher rates than saline marshes due to relatively lower soil strength (Valentine et al., 2021), which may explain much of the interior wetland loss relative to more coastal areas shown in Figure 5. With an inland shift of estuarine influence with RSLR, increased salinity will more strongly impact wetland growth due to the effects of salt as well as altered nutrient regimes (Krauss et al., 2009). The increased frequency of tidal inundation encourages salt-tolerant plants to colonize wetland soil environments that see increased brackish water. The prevalence of increasingly brackish water towards a tidal wetland's terrestrial edge inevitably sees salt-tolerant low-marsh species to outcompete the typically complex mosaic of upland marsh species that require higher levels of freshwater input (Hussein et al., 2004). Subdividing the estimated accretion rates by hydrologic basin reveals a clear association between the accretion rates in each basin and the land lost from 1984 to 2020 ( $R^2 = 0.630, p = 0.006$ ), with the basins with the highest accretion rates being freshwater deltaic environments. Further, these basins with the most loss largely align with the greatest decreases in estimated accretion rates from 1984 to 2020 (Figure 6). This relationship underscores accretion's importance in counteracting subsidence and erosion to prevent wetland submergence, and our modelling approach here allows for further interpretation of the wetland characteristics and mechanisms that influence accretion.

Quantifying nonlinear relationships and interactions between the dependent variables is key to the accretion model's success, as ecological patterns such as accretion often involve nonlinear and interactive processes (Ryo & Rillig, 2017). For example, as the distribution of accretion rates across Louisiana's coast varies by hydrologic

basin, the basins themselves have different dynamics pertaining to inorganic sedimentation and organic matter deposition. The Atchafalaya and Mississippi River Delta basins, being the primary outlets of the Mississippi River tributary network, are dominated by the river's sediment load passing through their major discharging outlets and aggrading within their deltaic wetlands (Olson & Suski, 2021). As wetlands in the remaining coastal basins have largely been isolated from the Mississippi River and its tributaries, they are more reliant on tidal sedimentation to deliver inorganic material to accrete surficial material. While model eight overall attains a relatively high  $R^2$  of 0.586 and a low MAE of 0.333 cm/year, the bias present in the scatterplot of modeled versus measured accretion rates (Figure 3) is likely due to the variation in hydrogeomorphic settings across the coastal basins and the different inorganic and organic deposition patterns entailed in each. It should be noted that while a per-basin modeling approach here did not yield appropriate results due to smaller sample sizes not capturing sufficient variation compared to the single coastwide model, future studies may take these varying hydrogeomorphic dynamics into consideration.

Testing several models with different variable combinations allows us to interpret which data inputs are more important for representing accretionary processes. In addition to overall and validation error metrics, the feature importance scores generated by each model quantify each variable's contribution to the accretion model in concert with the other utilized variables (Menze et al., 2009). Beyond mean TSS and NDVI in each CRMS site's 1 km radius, the selection of variables across all models (Table 1; mean distance to water, mean elevation, wetland vegetation class, and land:water pixel ratio) potentially capture information about accretionary processes and inform our model interpretation. Together, FMM distance and elevation—with feature importance scores of 0.200 and 0.208, respectively—improved the accretion model validation metrics in model 8 compared to other variable combinations. With these variables' feature importance scores being on par with TSS, these model metrics indicate that distance to water and elevation improved the model's accounting of accretion at the CRMS sites. This is likely due to distance and elevation in combination controlling the availability of sediment-bearing floodwaters in wetland vegetation, as well as elevation correlating with hydroperiod which in turn regulates vegetation productivity (Twilley et al., 2019). Conversely, the vegetation class variable attained low feature importance scores in each tested model, such that it contributed little to increased accuracy or introduced noise by not being closely related to organic matter deposition or sediment attenuation potential. Further, the land:water pixel ratio variable acts as a measure of marsh fragmentation, with a higher portion of water pixels in the 1 km radius indicating a less productive and more flood-prone environment that limits accretion potential. Models employing this ratio as a variable show that it attains feature importance scores on par with FMM distance and elevation, with models 5 and 9 among the top overall  $R^2$  and MAE scores. However, validation of these models show higher error than model 8, meaning that this ratio as a proxy for wetland fragmentation is redundant with or overall less accurate than using solely distance to water and elevation to simulate capture suspended sediment deposition at the sample sites.

One significant area for improvement on our generalized approach regarding sediment deposition is accounting for water's flow through wetland vegetation. This study specifically leverages Landsat to establish a relationship between the primary accretionary components (organic matter and inorganic sediment deposition), but there are complex factors such as river discharge, tidal influence, storm activity, vegetation community assemblage, and aboveground biomass that influence total accretion. These factors can have a significant bearing on how much organic matter is captured via litterfall and root turnover (Kirwan & Megonigal, 2013; Morris et al., 2012; Mudd et al., 2009), as well as how much suspended sediment is attenuated by vegetation (Krauss et al., 2014). Storm activity, being a significant short-term driver of wetland flooding and sediment deposition, also likely drives a portion of the sediment deposition across the coast (Twilley et al., 2019). While storm-driven sediment deposits are likely present in the CRMS accretion totals, storm activity is outside the scope of our longer-term timeseries study and likely induces some of the bias and noise in the model. The differences in accretionary dynamics across Louisiana's coastal basins likely explain the additional bias inherent in the accretion estimates, such that the distribution of modeled versus measured accretion rates skew from the 1:1 line with a slight overestimation at the low end of the scale and a slight underestimation at the high end (Figure 3). For example, the two westernmost coastal basins (Calcasieu/Sabine and Mermentau) have low average accretion rates but have relatively stable wetland area, with lower net rates of land loss compared to several of the eastern basins. Incorporating additional hydrogeomorphic data into the accretion modeling process may account for this and reduce error.

## 5. Conclusions

Here, we establish that vertical accretion—the building of surficial material within a wetland—can be modeled and estimated with optical remote sensing data. Enabled by cloud computing to process and export vast quantities of optical satellite data across coastal Louisiana, we leveraged a timeseries of Landsat data that spatially and temporally matches the public accretion record provided by the Coastwide Reference Monitoring System. We used these data to develop proxies for the primary accretionary factors, with local mean NDVI over each sample's timeframe simulating bioproductivity and organic matter deposition while mean TSS estimates within local water pixels estimated inorganic suspended sediment deposition. The application of machine learning-based Random Forest regression ingesting these remotely sensed data detected a significant relationship, which was improved by the addition of elevation and distance variables to better simulate sediment deposition.

Future remote sensing-based studies that estimate or integrate accretion and its contributing processes can make use of a wider array of biophysical and hydrologic input data. This study leveraged a timeseries of optical data to estimate accretionary processes, but other remote sensing platforms and datasets may be able to more directly measure those individual processes and integrated into a unified accretion model. For example, different airborne radar products have been applied for estimating total river discharge (Altenau et al., 2017; Fayne et al., 2020; Tuozzolo et al., 2019) and the detection of the water surface and its flow through wetland vegetation (Liao et al., 2020). Additionally, airborne imaging spectrometer data has a demonstrated ability to derive accurate and transferable estimates of suspended sediment concentrations (Jensen, Simard, et al., 2019), as well as being able to map vegetation types and aboveground biomass (Jensen, Cavanaugh, Simard et al., 2019, 2021). These various airborne instruments and their datasets will be unified in NASA's Delta-X Earth Venture Suborbital mission (<https://deltax.jpl.nasa.gov/>) to develop a regional process-based accretion model in coastal Louisiana. Looking to the future, spaceborne remote sensing platforms informed by airborne counterparts and their applications—including Surface Water Ocean Topography (Fu et al., 2012), NASA-ISRO Synthetic Aperture Radar (Kellog et al., 2020), and Surface Biology and Geology (Cawse-Nicholson et al., 2021)—will enable analysis of accretion and its constituent processes globally. In doing so, we will be able to make global assessments of coastal wetland productivity and vulnerability.

## Conflict of Interest

The authors declare no conflicts of interest relevant to this study.

## Data Availability Statement

Data presented in this study are available through public resources. CRMS accretion data are available via the CPRA website (<https://cims.coastal.louisiana.gov/monitoring-data>), as well as the corresponding CRMS site GIS point layer and the hydrologic basin layer ([https://lacoast.gov/crms\\_viewer/Map/CRMSViewer](https://lacoast.gov/crms_viewer/Map/CRMSViewer)). In situ TSS and remote sensing reflectance sample data (Castaneda et al., 2020; Jensen et al., 2020) used for TSS model selection (Figure 2) are available via the ORNL DAAC Delta-X data portal ([https://daac.ornl.gov/cgi-bin/dataset\\_lister.pl?p=41](https://daac.ornl.gov/cgi-bin/dataset_lister.pl?p=41)). Landsat data are available via Google Earth Engine (<https://earthengine.google.com/>) or the USGS EarthExplorer (<https://earthexplorer.usgs.gov/>).

## References

- Allison, M. A., Demas, C. R., Ebersole, B. A., Kleiss, B. A., Little, C. D., Meselhe, E. A., et al. (2012). A water and sediment budget for the lower Mississippi-Atchafalaya River in flood years 2008-2010: Implications for sediment discharge to the oceans and coastal restoration in Louisiana. *Journal of Hydrology*, 432–433(February), 84–97. <https://doi.org/10.1016/j.jhydrol.2012.02.020>
- Altenau, E. H., Pavelsky, T. M., Moller, D., Lion, C., Pitcher, L. H., Allen, G. H., et al. (2017). AirSWOT measurements of river water surface elevation and slope: Tanana River, AK. *Geophysical Research Letters*, 44(1), 181–189. <https://doi.org/10.1002/2016GL071577>
- Barras, J., Beville, S., Britsch, D., Hartley, S., Hawes, S., Johnston, J., et al. (2003). *Historical and projected coastal Louisiana land changes: 1978-2050* (Vol. 334). Retrieved from <http://www.louisianaspeaks-parishplans.org/projectattachments/001246/NewHistoricalland.pdf>
- Baustian, M. M., Stagg, C. L., Perry, C. L., Moss, L. C., & Carruthers, T. J. B. (2021). Long-term carbon sinks in marsh soils of coastal Louisiana are at risk to wetland loss. *Journal of Geophysical Research*. <https://doi.org/10.1029/2020JG005832>
- Baustian, M. M., Stagg, C. L., Perry, C. L., Moss, L. C., Carruthers, T. J. B., & Allison, M. (2017). Relationships between salinity and short-term soil carbon accumulation rates from marsh types across a landscape in the Mississippi River Delta. *Wetlands*, 37(2), 313–324. <https://doi.org/10.1007/s13157-016-0871-3>

## Acknowledgments

This work was carried out at the Jet Propulsion Laboratory, California Institute of Technology, under a contract with the National Aeronautics and Space Administration (80NM0018D0004). Jensen was supported by the NASA Postdoctoral Program. Simard, Fagherazzi, and Cortese were funded by the NASA Delta-X project. Delta-X is funded by the Science Mission Directorate's Earth Science Division through the Earth Venture Suborbital-3 Program NNH17ZDA001N-EVS3. This study further benefited from the Coastwide Reference Monitoring System (CRMS) Program's long-term monitoring network, funded by the Coastal Wetland Planning, Protection, and Restoration Act Program and the State of Louisiana. © 2022. All rights reserved.



- Breda, A., Saco, P. M., Sandi, S. G., Saintilan, N., Riccardi, G., & José, F. (2020). Accretion, retreat and transgression of coastal wetlands experiencing sea-level rise. *Hydrology and Earth System Sciences*, 439(September), 1–22.
- Burkett, V. R., Ziklowski, D. B., & Hart, D. A. (2003). Sea-level rise and subsidence: Implications for flooding in New Orleans, Louisiana. *U.S. Geological Survey Subsidence Interest Group Conference: Proceedings of the Technical Meeting, Galveston, Texas, November, 27–29(2001)*, 63–70.
- Byrd, K. B., Ballanti, L., Thomas, N., Nguyen, D., Holmquist, J. R., Simard, M., & Windham-Myers, L. (2018). A remote sensing-based model of tidal marsh aboveground carbon stocks for the conterminous United States. *ISPRS Journal of Photogrammetry and Remote Sensing*, 139, 255–271. <https://doi.org/10.1016/j.isprsjprs.2018.03.019>
- Cahoon, D. R., White, D. A., & Lynch, J. C. (2011). Sediment infilling and wetland formation dynamics in an active crevasse splay of the Mississippi River delta. *Geomorphology*, 131(3–4), 57–68. <https://doi.org/10.1016/j.geomorph.2010.12.002>
- Castaneda, E., Christensen, A. I., Simard, M., Jensen, D. J., Twilley, R., & Lane, R. (2020). *Pre-Delta-X: Total suspended solids of surface water across MRD, LA, USA, 2015–2016*. ORNL DAAC. <https://doi.org/10.3334/ORNLDAAC/1802>
- Cawse-Nicholson, K., Townsend, P. A., Schimel, D., Assiri, A. M., Blake, P. L., Fabrizio, M., et al. (2021). NASA's surface biology and geology designated observable: A perspective on surface imaging algorithms. *Remote Sensing of Environment*, 257, 112349. <https://doi.org/10.1016/j.rse.2021.112349>
- Chen, S., Han, L., Chen, X., Li, D., Sun, L., & Li, Y. (2015). Estimating wide range Total Suspended Solids concentrations from MODIS 250-m imagery: An improved method. *ISPRS Journal of Photogrammetry and Remote Sensing*, 99, 58–69. <https://doi.org/10.1016/j.isprsjprs.2014.10.006>
- Chmura, G. L., Anisfeld, S. C., Cahoon, D. R., & Lynch, J. C. (2003). Global carbon sequestration in tidal, saline wetland soils. *Global Biogeochemical Cycles*, 17(4). <https://doi.org/10.1029/2002GB001917>
- Cortese, L., & Fagherazzi, S. (2022). Fetch and distance from the bay control accretion and erosion patterns in Terrebonne marshes (Louisiana, USA). *Earth Surface Processes and Landforms*. <https://doi.org/10.1002/esp.5327>
- Couvillion, B. R. (2021). *Coastal wetland area change in the Gulf of Mexico, 1985–2020*. U.S. Geological Survey data release. <https://doi.org/10.5066/P9ZQ17ZW>
- Craft, C., Clough, J., Ehman, J., Jove, S., Park, R., Pennings, S., et al. (2009). Forecasting the effects of accelerated sea-level rise on tidal marsh ecosystem services. *Frontiers in Ecology and the Environment*, 7(2), 73–78. <https://doi.org/10.1890/070219>
- Day, J. W., Boesch, D. F., Clairain, E. J., Kemp, G. P., Laska, S. B., Mitsch, W. J., et al. (2007). Restoration of the Mississippi delta: Lessons from Hurricanes Katrina and Rita. *Science*, 315(5819), 1679–1684. <https://doi.org/10.1126/science.1137030>
- Day, J. W., Conner, W. H., Delaune, R. D., Hopkinson, C. S., Hunter, R. G., Shaffer, G. P., et al. (2021). A review of 50 Years of study of Hydrology, wetland dynamics, aquatic Metabolism, water quality and Trophic Status, and nutrient Biogeochemistry in the Barataria basin, Mississippi delta — system functioning, human impacts and restoration Approaches. *Water*, 13(642), 1–32. <https://doi.org/10.3390/w13050642>
- Dogliotti, A. I., Ruddick, K. G., Nechad, B., Doxaran, D., & Knaeps, E. (2015). A single algorithm to retrieve turbidity from remotely-sensed data in all coastal and estuarine waters. *Remote Sensing of Environment*, 156, 157–168. <https://doi.org/10.1016/j.rse.2014.09.020>
- Dorji, P., & Fearn, P. (2016). A quantitative comparison of total suspended sediment algorithms: A case study of the last decade for MODIS and landsat-based sensors. *Remote Sensing*, 8(10). <https://doi.org/10.3390/rs8100810>
- Doughty, C. L., & Cavanaugh, K. C. (2019). Mapping coastal wetland biomass from high resolution unmanned aerial vehicle (UAV) imagery. *Remote Sensing*, 11(5). <https://doi.org/10.3390/rs11050540>
- Ericson, J. P., Vörösmarty, C. J., Dingman, S. L., Ward, L. G., & Meybeck, M. (2006). Effective sea-level rise and deltas: Causes of change and human Dimension Implications. *Global and Planetary Change*, 50(1–2), 63–82. <https://doi.org/10.1016/j.gloplacha.2005.07.004>
- Fayne, J. V., Smith, L. C., Pitcher, L. H., Kyzivat, E. D., Cooley, S. W., Cooper, M. G., et al. (2020). Airborne observations of arctic-boreal water surface elevations from AirSWOT Ka-Band InSAR and LVIS LiDAR. *Environmental Research Letters*, 15(10). <https://doi.org/10.1088/1748-9326/abadcc>
- FitzGerald, D. M., Fenster, M. S., Argow, B. A., & Buynevich, I. V. (2008). Coastal impacts due to sea-level rise. *Annual Review of Earth and Planetary Sciences*, 36(1), 601–647. <https://doi.org/10.1146/annurev.earth.35.031306.140139>
- Fu, L.-L., Alsdorf, D., Morrow, R., Rodriguez, E., & Mognard, N. (2012). *Swot: The surface water and Ocean Topography mission wide-Swath Altimetric measurement of water elevation on Earth*. JPL Publication.
- Goodbred, S. L., & Hine, A. C. (1995). Coastal storm deposition: Salt-marsh response to a severe extratropical storm, March 1993, west-central Florida. *Geology*, 23(8), 679–682. [https://doi.org/10.1130/0091-7613\(1995\)023<0679:CSDSMR>2.3.CO;2](https://doi.org/10.1130/0091-7613(1995)023<0679:CSDSMR>2.3.CO;2)
- Goodwin, G. C. H., & Mudd, S. M. (2019). High platform elevations highlight the role of storms and spring tides in salt marsh evolution. *Frontiers in Environmental Science*, 7(May), 1–14. <https://doi.org/10.3389/fenvs.2019.00062>
- Griffin, C. G., Frey, K. E., Rogan, J., & Holmes, R. M. (2011). Spatial and Interannual Variability of dissolved organic matter in the Kolyma river, East Siberia, observed using satellite imagery. *Journal of Geophysical Research*, 116(3), 1–12. <https://doi.org/10.1029/2010JG001634>
- Hussein, A. H., Rabenhorst, M. C., & Tucker, M. L. (2004). Modeling of carbon sequestration in coastal marsh soils. *Soil Science Society of America Journal*, 68(5), 1786. <https://doi.org/10.2136/sssaj2004.1786>
- Jensen, D., Cavanaugh, K. C., Simard, M., Christensen, A., Rovai, A., & Twilley, R. (2021). Aboveground biomass distributions and vegetation composition changes in Louisiana's Wax Lake Delta. *Estuarine, Coastal and Shelf Science*, 250(March 2021), 107139. <https://doi.org/10.1016/j.ecss.2020.107139>
- Jensen, D., Cavanaugh, K. C., Simard, M., Okin, G. S., Castañeda-Moya, E., McCall, A., & Twilley, R. R. (2019). Integrating imaging spectrometer and Synthetic Aperture radar data for estimating wetland vegetation aboveground biomass in coastal Louisiana. *Remote Sensing*, 11(21), 2533. <https://doi.org/10.3390/rs11212533>
- Jensen, D., Simard, M., Cavanaugh, K., Sheng, Y., Fichot, C. G., Pavelsky, T., & Twilley, R. (2019). Improving the transferability of suspended solid estimation in wetland and deltaic waters with an empirical hyperspectral approach. *Remote Sensing*, 11(13), 1629. <https://doi.org/10.3390/rs11131629>
- Jensen, D. J., Pavelsky, T. M., & Lion, C. (2020). *Pre-Delta-X: Spectral reflectance of water surface, Atchafalaya Basin, LA, USA, 2016*. ORNL DAAC. <https://doi.org/10.3334/ORNLDAAC/1804>
- Kellogg, K., Rosen, P., Barela, P., Hoffman, P., Edelstein, W., Standley, S., et al. (2020). *NASA-ISRO Synthetic Aperture Radar (NISAR) Mission*. Paper Presented at IEEE Aerospace Conference, IEEE. <https://doi.org/10.1109/aero47225.2020.9172638>
- Kim, W., Mohrig, D., Twilley, R. R., Paola, C., & Parker, G. (2009). Is it feasible to build new land in the Mississippi River Delta? *Eos Trans. American Geophysical Union*, 90(42), 373–374. <https://doi.org/10.1029/2009eo420001>
- Kirwan, M. L., & Guntenspergen, G. R. (2010). Influence of tidal range on the stability of coastal marshland. *Journal of Geophysical Research*, 115(F2), 1–11. <https://doi.org/10.1029/2009JF001400>

- Kirwan, M. L., & Megonigal, J. P. (2013). Tidal wetland stability in the face of human impacts and sea-level rise. *Nature*, 504(7478), 53–60. <https://doi.org/10.1038/nature12856>
- Krauss, K. W., Duberstein, J. A., Doyle, T. W., Conner, W. H., Day, R. H., Inabinette, L. W., & Whitbeck, J. L. (2009). Site condition, structure, and growth of baldcypress along tidal/non-tidal salinity gradients. *Wetlands*, 29(2), 505–519. <https://doi.org/10.1672/08-77.1>
- Krauss, K. W., McKee, K. L., Lovelock, C. E., Cahoon, D. R., Saintilan, N., Reef, R., & Chen, L. (2014). How mangrove forests adjust to rising sea level. *New Phytologist*, 202(1), 19–34. <https://doi.org/10.1111/nph.12605>
- Liao, T., Simard, M., Denbina, M., & Lamb, M. P. (2020). Monitoring water level change and seasonal vegetation change in the coastal wetlands of Louisiana using L-band time-series. *Remote Sensing*, 12(2351), 1–24. <https://doi.org/10.3390/rs12152351>
- Liu, Z., Fagherazzi, S., & Cui, B. (2021). Success of coastal wetlands restoration is driven by sediment availability Zezheng. *Communications Earth & Environment*, 2(44), 1–9. <https://doi.org/10.1038/s43247-021-00117-7>
- Menze, B. H., Kelm, B. M., Masuch, R., Himmelreich, U., Bachert, P., Petrich, W., & Hamprecht, F. A. (2009). A comparison of random forest and its Gini importance with standard chemometric methods for the feature selection and classification of spectral data. *BMC Bioinformatics*, 10, 1–16. <https://doi.org/10.1186/1471-2105-10-213>
- Mobley, C., Boss, E., & Roesler, C. (2010). *Ocean optics web book*. [Online]. Retrieved from <http://www.oceanopticsbook.info/>
- Morris, J. T., Edwards, J., Crooks, S., & Reyes, E. (2012). Assessment of carbon sequestration potential in coastal wetlands. In R. Lal, K. Lorenz, R. F. Huttel, B. U. Schneider, & J. von Braun (Eds.), *Recarbonization of the biosphere: Ecosystems and the global carbon cycle* (1st ed., pp. 517–531). Springer. <https://doi.org/10.1007/978-94-007-4159-1>
- Morris, J. T., Sundareshwar, P. V., Nietch, C. T., Kjerfve, B., & Cahoon, D. R. (2002). Responses of coastal wetlands to rising sea level. *Ecology*, 83(10), 2869–2877. [https://doi.org/10.1890/0012-9658\(2002\)083\[2869:rocwtr\]2.0.co;2](https://doi.org/10.1890/0012-9658(2002)083[2869:rocwtr]2.0.co;2)
- Morton, R., Bernier, J., & Barras, J. (2006). Evidence of regional subsidence and associated interior wetland loss induced by hydrocarbon production, Gulf Coast region, USA. *Environmental Geology*, 50(2), 261–274. <https://doi.org/10.1007/s00254-006-0207-3>
- Mudd, S. M., Howell, S. M., & Morris, J. T. (2009). Impact of dynamic feedbacks between sedimentation, sea-level rise, and biomass production on near-surface marsh stratigraphy and carbon accumulation. *Estuarine, Coastal and Shelf Science*, 82(3), 377–389. <https://doi.org/10.1016/j.ecss.2009.01.028>
- Nechad, B., Ruddick, K. G., & Park, Y. (2010). Calibration and validation of a generic multisensor algorithm for mapping of total suspended matter in turbid waters. *Remote Sensing of Environment*, 114(4), 854–866. <https://doi.org/10.1016/j.rse.2009.11.022>
- Olmanson, L. G., Brezonik, P. L., & Bauer, M. E. (2013). Airborne hyperspectral remote sensing to assess spatial distribution of water quality characteristics in large rivers: The Mississippi river and its tributaries in Minnesota. *Remote Sensing of Environment*, 130, 254–265. <https://doi.org/10.1016/j.rse.2012.11.023>
- Olson, K. R., & Suski, C. D. (2021). Mississippi River Delta: Land subsidence and coastal erosion. *Open Journal of Soil Science*, 11, 139–163. <https://doi.org/10.4236/ojss.2021.113008>
- Pereira, L. S. F., Andes, L. C., Cox, A. L., & Ghulam, A. (2018). Measuring suspended-sediment concentration and turbidity in the middle Mississippi and lower Missouri rivers using landsat data. *Journal of the American Water Resources Association*, 54(2), 440–450. <https://doi.org/10.1111/1752-1688.12616>
- Rangoonwala, A., Jones, C. E., & Ramsey, E. (2016). Wetland shoreline recession in the Mississippi River delta from petroleum oiling and cyclonic storms. *Geophysical Research Letters*, 43(22), 11652–11660. <https://doi.org/10.1002/2016GL070624>
- Roy, S., Robeson, S. M., Ortiz, A. C., & Edmonds, D. A. (2020). Spatial and temporal patterns of land loss in the Lower Mississippi River Delta from 1983 to 2016. *Remote Sensing of Environment*, 250(August), 112046. <https://doi.org/10.1016/j.rse.2020.112046>
- Ryo, M., & Rillig, M. C. (2017). Statistically reinforced machine learning for nonlinear patterns and variable interactions. *Ecosphere*, 8(11). <https://doi.org/10.1002/ecs2.1976>
- Schoolmaster, D. R., Stagg, C. L., Sharp, L. A., McGinnis, T. E., Wood, B., & Piazza, S. C. (2018). Vegetation cover, tidal amplitude and land area predict short-term marsh vulnerability in coastal Louisiana. *Ecosystems*, 21(7), 1335–1347. <https://doi.org/10.1007/s10021-018-0223-7>
- Snedden, G. A., Cretini, K., & Patton, B. (2014). Inundation and salinity impacts to above- and belowground productivity in *Spartina patens* and *Spartina alterniflora* in the Mississippi River deltaic plain: Implications for using river diversions as restoration tools. *Ecological Engineering*, 81, 133–139. <https://doi.org/10.1016/j.ecoleng.2015.04.035>
- Song, C., White, B. L., & Heumann, B. W. (2011). Hyperspectral remote sensing of salinity stress on red (*Rhizophora mangle*) and white (*Laguncularia racemosa*) mangroves on Galapagos Islands. *Remote Sensing Letters*, 2(3), 221–230. <https://doi.org/10.1080/01431161.2010.514305>
- Thomas, N., Simard, M., Cateñeda-Moya, E., Byrd, K., Windham-Myers, L., Bevington, A., & Twilley, R. R. (2019). High-resolution mapping of biomass and distribution of marsh and forested wetlands in southeastern coastal Louisiana. *International Journal of Applied Earth Observation and Geoinformation*, 80(December2018), 257–267. <https://doi.org/10.1016/j.jag.2019.03.013>
- Tognin, D., D'Alpaos, A., Marani, M., & Carniello, L. (2021). Marsh resilience to sea-level rise reduced by storm-surge barriers in the Venice Lagoon. *Nature Geoscience*, 14(12), 906–911. <https://doi.org/10.1038/s41561-021-00853-7>
- Topp, S. N., Pavelsky, T. M., Jensen, D., Simard, M., & Ross, M. R. V. (2020). Research trends in the use of remote sensing for inland water quality science: Moving towards multidisciplinary applications. *Water*, 12(1), 1–34. <https://doi.org/10.3390/w12010169>
- Tuozzolo, S., Lind, G., Overstreet, B., Mangano, J., Fonstad, M., Hagemann, M., et al. (2019). Estimating river discharge with Swath Altimetry: A Proof of Concept using AirSWOT observations. *Geophysical Research Letters*, 46(3), 1459–1466. <https://doi.org/10.1029/2018GL080771>
- Twilley, R. R., Bentley, S. J., Chen, Q., Edmonds, D. A., Hagen, S. C., Lam, N. S. N., et al. (2016). Co-evolution of wetland landscapes, flooding, and human settlement in the Mississippi River Delta Plain. *Sustainability Science*, 11(4), 711–731. <https://doi.org/10.1007/s11625-016-0374-4>
- Twilley, R. R., Day, J. W., Bevington, A. E., Castañeda-moya, E., Christensen, A., Holm, G., et al. (2019). Ecogeomorphology of coastal deltaic floodplains and estuaries in an active delta: Insights from the Atchafalaya Coastal Basin. *Estuarine, Coastal and Shelf Science*, 227(August). <https://doi.org/10.1016/j.ecss.2019.106341>
- Valentine, K., Bruno, G., Elsey-Quirk, T., & Mariotti, G. (2021). Brackish marshes erode twice as fast as saline marshes in the Mississippi Delta region. *Earth Surface Processes and Landforms*, 46(9), 1739–1749. <https://doi.org/10.1002/esp.5108>
- Vanhellemont, Q., & Ruddick, K. (2014). Turbid wakes associated with offshore wind turbines observed with Landsat 8. *Remote Sensing of Environment*, 145, 105–115. <https://doi.org/10.1016/j.rse.2014.01.009>
- Zhang, X., Xu, K., Yang, Z., Tan, X., & Wu, C. (2021). Decreasing land growth and unique seasonal area fluctuations of two newborn Mississippi subdeltas. *Geomorphology*, 378, 107617. <https://doi.org/10.1016/j.geomorph.2021.107617>